



Effect of ball peening of substrate on microstructure, phase evolution and properties of electrophoretically deposited YSZ/(Ni, Al) composite coatings

Shan-guang SONG, Shi-lei TAN, Xiao-xiao QI, Wei WANG, Li-li WANG

School of Materials Engineering, Shanghai University of Engineering Science, Shanghai 201620, China

Received 10 October 2015; accepted 25 February 2016

Abstract: YSZ/(Ni, Al) composite coatings were deposited on Inconel600 superalloy with ball peening (BP) and without (non BP) treatment using the electrophoretic deposition (EPD) technique, followed by vacuum sintering method. The structures and phase evolution of the coatings were studied with X-ray diffraction (XRD), scanning electron microscopy (SEM) and energy dispersive spectrometry (EDS). The relation between microstructures and properties of the BPs-coated samples was discussed. The results show that the adhesion strength and gain mass of the BPs-coated samples with isothermal oxidation at 1100 °C for 100 h are 3.3 N and 0.00817 mg/cm², respectively, while those of the non-BPs-coated sample are 2.6 N and 0.00559 mg/cm², respectively. The EDS mapping analysis indicates that an obvious outward diffusion of Cr from the substrate to BPs coated samples occurs after isothermal oxidation. The BPs-coated sample shows the superior adhesion and oxidation resistance compared with non-BPs-coated samples.

Key words: composite coatings; electrophoretic deposition; ball peening treatment; adhesion strength; high temperature oxidation resistance

1 Introduction

Yttria-stabilized zirconia (YSZ) has been widely used as thermal barrier coating (TBC) to provide thermal insulation for metallic components against the hot gas stream in gas turbine engines used for aircraft, propulsion, and power generation [1]. The currently used YSZ coatings are deposited by electron beam physical vapor deposition (EB-PVD) [2,3] or air plasma spray (APS) [4,5]. While these techniques are applied with great success, they are cost and time intensive, and the coating of complex shapes may be difficult or even impossible. The electrophoretic deposition (EPD) technique, with range of novel applications in the processing of advanced ceramic materials and coatings, has recently gained increasing interest because of not only the high versatility of its use with different materials but also its cost-effectiveness requiring simple apparatus [6–8]. However, the main problem associated with EPD technique is the volume shrinkage of the coatings during sintering, which leads to the formation of cracks in the coatings. YSZ/Al and YSZ/(Ni,Al) EPD composite coatings have been developed to produce

net-shape ceramics, which overcome problems caused by shrinkage of ceramics during sintering [9,10]. YSZ/Al and YSZ/(Ni,Al) composite coatings can be modified in various ways by incorporating metal (Ni and Al) and ceramic additives to change the final composite composition, to accelerate the reaction, to further compensate for the sintering shrinkage. Successful coatings require good bonding between the coating and the substrate. Inter-diffusion of elemental components of YSZ/(Ni,Al) coating and the superalloy substrate to form a region of continuous chemical bonding near the interface has been documented in the previous study [10]. This bonding should provide additional strength to the interface region between YSZ/(Ni,Al) composite coatings and the substrate. Moreover, formation of continuous chemical bonding is also favorable for reducing the coefficient of thermal expansion between the composite coatings and the substrate and improving the interface adhesion behavior of composite coatings/substrate. It is well known that plastic deformation of substrate can cause a large amount of structure defects [11]. Structure defects can obviously influence the atomic constituents of the substrate inter-diffusion, which will react over a region close to the composite

coating-substrate interface that will consequently have an impact on the properties of composite coatings. However, the effect of ball peening of substrate on element inter-diffusion, adhesion strength and oxidation resistance of YSZ/(Ni,Al) composite coatings has not been studied.

The purpose of this work is to study the effect of ball peening of substrate on element inter-diffusion, adhesion strength and oxidation resistance of YSZ/(Ni,Al) composite coatings, and report the results of chemical analysis and phase structures at composite coatings-substrate interface by EDS elements mapping and micro-XRD analysis.

2 Experimental

In this work, Ni-based superalloy (Inconel 600) was used as the substrate mainly composed of 72% Ni, 14%–16% Cr, 6%–10% Fe, 0.15% C, 1% Mn, 0.5% Si, and 0.3% Al. The substrate was cut into samples with dimensions of 10 mm × 10 mm × 3 mm. The samples were ground using a QM-15 Mixer Mill [12]. In order to ensure an approximately uniform distribution of impacts, the container was filled with a large number of SiC milling balls. Milling experiments were carried out by using 100 balls with different diameters of 10, 5, 3 and 1 mm for 10 h, the corresponding ratios of the number of the balls are 20%, 20%, 30% and 30% [13], respectively. Subsequently, the samples were cleaned thoroughly with acetone. A mixture of 92% YSZ powder, 4% Al and 4% Ni powder (powder of YSZ, Al and Ni from Aladdin company) suspension was diluted in acetyl acetone to a solid concentration of 40 g/L. After vibrating about 5 to 10 min, adding 0.4 g/L iodine, and followed by continuous stirring for 2–3 h. The suspension was prepared by adding a drop of polyvinyl alcohol as suspension stabilization additive to disperse powders and reduce agglomeration. EPD was carried out with electric field applied between a graphite counter (anode) and a Inconel 600 substrate (cathode). The distance between the two electrodes was 30 mm. Applied voltage and deposition time were 160 V and 2 min, respectively. The green coatings were dried in air at room temperature for 24 h before their further densification step. The sintering of EPD-coated samples was performed at 1100 °C for 2 h under vacuum (6.67 mPa) and then furnace cooled to room temperature.

To study high temperature oxidation resistance, the as-sintered composite coatings were further oxidized at 1100 °C for 100 h in static air followed by air cooling. The bonding strength of coating was tested with a WS-2006 type thin film adhesion automatic scratch tester, the load of 40 N, loading rate of 20 N/min, scratch length of 2 min, and scratch speed of 2 mm/s. The phase structures, microstructure and composition of YSZ/

(Al,Ni) composite coatings were characterized by X-ray diffraction (XRD), scanning electron microscopy (SEM) and energy dispersive spectrometry (EDS), respectively.

3 Result

3.1 Structural characterization of composite coatings

The surface morphology and microstructure of YSZ/(Ni, Al) composite coatings without ball peening of the substrate (non BPs) after vacuum sintering and isothermal oxidation are shown in Figs. 1(a)–(c). Compared with non-BPs-coated samples, it can be seen that the top surface of YSZ/(Ni, Al) composite coatings after ball peening of the substrate (BPs) is relatively dense as shown in Figs. 1(a) and (d); no obvious cracks are found on the BPs-coated samples after vacuum sintering and isothermal oxidation, as shown in Figs. 1(d)–(f). Comparing the SEM images of non-BPs- and BPs-coated samples, it is apparent that BPs-coated samples exhibited more homogeneous and uniform surfaces than non-BPs-coated samples. Furthermore, Figs. 1(d) and (f) show that the particle size on the BPs-coated samples increases slightly with increasing oxidation time.

Figure 2 shows the cross-sectional microstructures of the non-BPs- and BPs-coated YSZ/(Ni, Al) samples oxidized at 1100 °C for 10 h and 100 h. It can be seen that the composite coatings have almost the same thickness in both cases, and around 40 μm in thickness (Fig. 2(a)). After vacuum sintering at 1100 °C for 2 h, a number of micron and submicron pores are homogeneously distributed on the non-BPs-coated samples (Fig. 2(a)). After isothermal oxidation at 1100 °C for 10 h and 100 h in air, some big cracks can be seen on the non-BPs-coated samples (Figs. 2(b) and (c)). In contrast, the BPs coating contained smaller irregular pores (Fig. 2(d)) and showed an adherence to the superalloy substrate without cracks or spallation (Figs. 2(e) and (f)). This indicates that the thermal expansion coefficient of the BPs-coated samples and the superalloy substrate matched each other very well after oxidation for 100 h. And it also means that BPs-coated samples will still be effective for a longer period of oxidation.

3.2 Phase composition and element distribution

Figure 3 shows the X-ray diffraction patterns of non-BPs- and BPs-coated YSZ/(Ni, Al) samples after vacuum sintering at 1100 °C for 2 h. After vacuum sintering at 1100 °C for 2 h, both AlNi₃ and cubic or/and tetragonal zirconia phases are observed in the XRD patterns. The mass of two phases is estimated by the quantitative phase analysis in X'Pert HighScore works on the basis of the RIR (reference intensity ratio) values [14]. The mass fraction of various phases w_i is

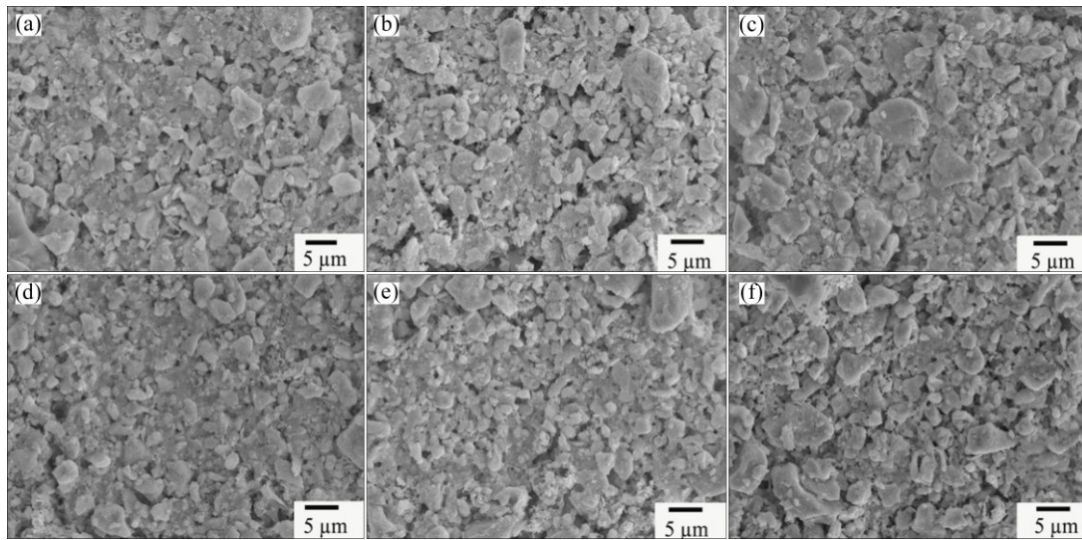


Fig. 1 SEM images of non-BPs-coated samples oxidized for 0 h (a), 10 h (b), 100 h (c) and BPs-coated samples oxidized for 0 h (d), 10 h (e), 100 h (f) at 1100 °C

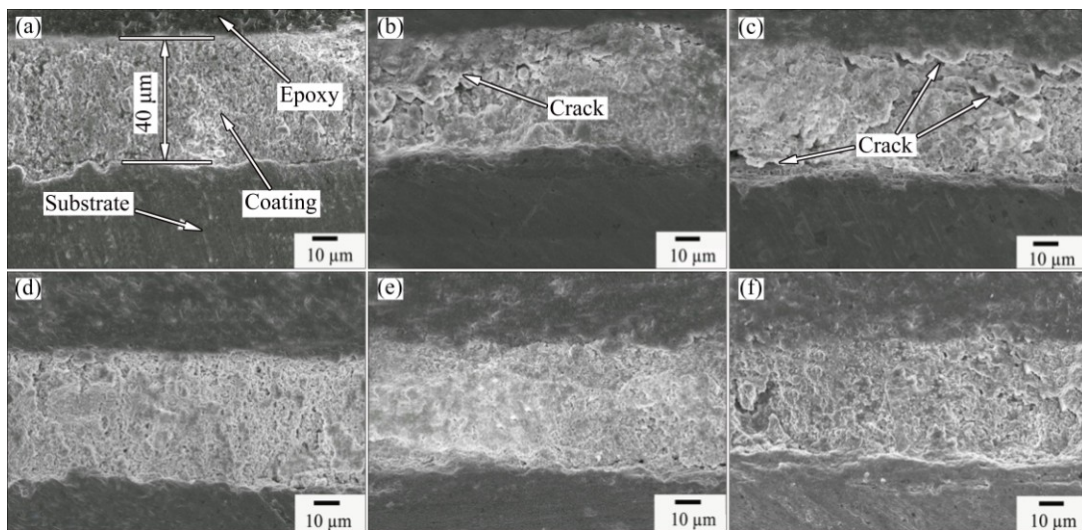


Fig. 2 Cross-sectional SEM images of non-BPs-coated samples oxidized for 0 h (a), 10 h (b), 100 h (c) and BPs-coated samples oxidized for 0 h (d), 10 h (e), 100 h (f) at 1100 °C

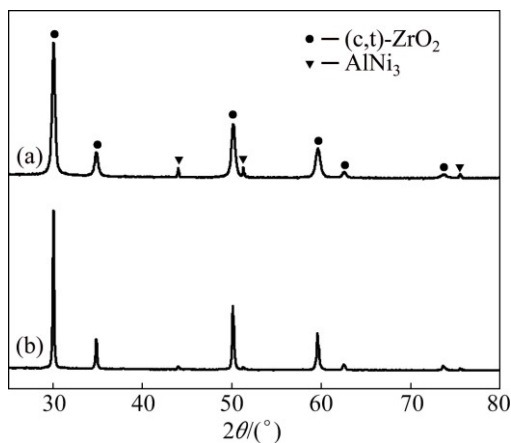


Fig. 3 XRD patterns of non-BPs- (a) and BPs-coated (b) YSZ/(Ni,Al) samples after vacuum sintering ($<10^{-3}$ Pa) at 1100 °C for 2 h

calculated using Eq. (1). K_i is the reference intensity of the i_{th} phase of the sample, and I_i is the intensity of the strongest peak of the i_{th} phase in the analyzed mixture. The comparison between non-BPs- and BPs-coated samples reveals that the mass fraction of $AlNi_3$ phase of BPs-coated sample is lower than that of non-BPs-coated samples. In comparison with the mass fraction of 5.5% for non-BPs-coated sample, the mass fraction of $AlNi_3$ phase for BPs-coated sample drops to 4.1%.

$$w_i = \left(\frac{K_i}{I_i} \sum_{t=1}^n \frac{i_t}{k_t} \right)^{-1} \quad (1)$$

Previous results indicate that non-BPs-coated samples mainly consist of cubic or/and tetragonal ZrO_2 , $AlNi_3$ phase and a minor of Al_2O_3 oxide after exposure in air at 1100 °C for 10 h, whereas cubic or/and tetragonal

ZrO₂, AlNi₃ phase and a minor of NiAl₂O₄ were detected after exposure in air for 100 h [10]. In the isothermal oxidation process from 10 to 100 h of the non-BPs-coated samples, the AlNi₃ was oxidated to Al₂O₃ and NiO, and then formed NiAl₂O₄.

Figure 4 shows the presence of cubic or/and tetragonal ZrO₂, AlNi₃ and a minor of NiO-phases on the BPs-coated samples after exposure in air for 10 h (Fig. 4(a)). In contrast, complex oxide products including cubic or/and tetragonal ZrO₂, Al₂O₃, Cr₂O₃ and NiCr₂O₄ were detected after exposure in air for 100 h (Fig. 4(b)). In the isothermal oxidation process from 10 h to 100 h of the BPs-coated samples, AlNi₃ and Cr were oxidated to Al₂O₃, Cr₂O₃ and NiO, and then Cr₂O₃ and NiO formed the NiCr₂O₄.

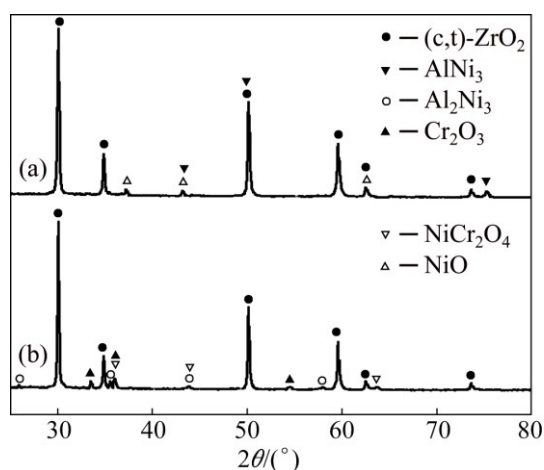


Fig. 4 XRD patterns of BPs-coated samples after isothermal oxidation in air at 1100 °C for 10 h (a) and 100 h (b)

In order to study the elemental distributions across the coatings–substrate region and the change in composition with oxidation time due to diffusion, SEM elemental mapping of the coatings–substrate region was carried out. Figure 5 shows the cross-sectional elemental mapping of Cr, Ni, Al and Fe obtained near the non-BPs- and BPs-coated samples–substrate interface after vacuum sintering at 1100 °C for 2 h. The distribution of the corresponding elements of non-BPs- and BPs-coated samples proves that there is no obvious diffusion of Cr, Ni, Al and Fe from the substrate to the composite coatings during vacuum sintering by taking into account the testing error.

Figures 6 and 7 show the cross-sectional elemental mapping of Cr, Ni, Al and Fe close to the non-BPs- and BPs-coated samples–substrate interface. It can be observed that outward diffusion of Cr from the substrate to coating resulted in the formation of Cr-rich transition-layer in the coating. After isothermal oxidation in air at 1100 °C for 10 h, Cr diffused into the BPs- and non-BPs-coated samples to depths of about 3.64 and 2.09 μm , respectively. The diffusion thickness increased with increasing oxidation time from 10 h to 100 h in both BPs- (4.0 μm) and non-BPs-coated (2.91 μm) samples. The diffusion depth of Cr diffused into the BPs-coated samples is thicker than that of the non-BPs-coated samples. The distribution of the corresponding elements indicates that there is no obvious diffusion of Fe and Ni from the substrate to the coating in both coated samples by taking into account the testing error. Al diffusing inward to the substrate is also not found. However, enrichment of Ni is identified at the interface between

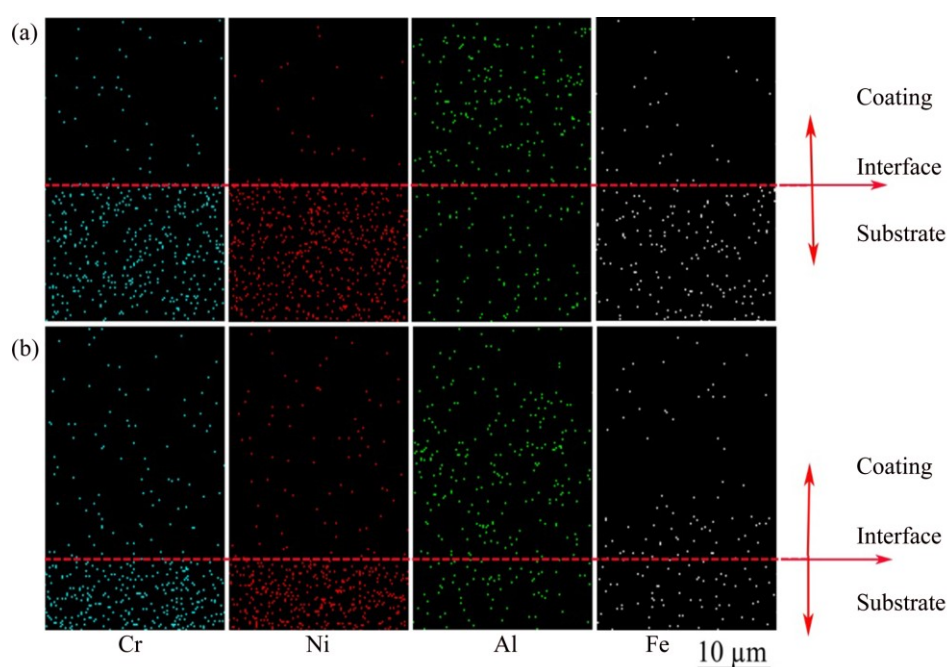


Fig. 5 Cross-sectional elemental distribution mapping of Cr, Ni, Al and Fe elements of non-BPs- (a) and BPs-coated (b) samples after vacuum sintering at 1100 °C for 2 h

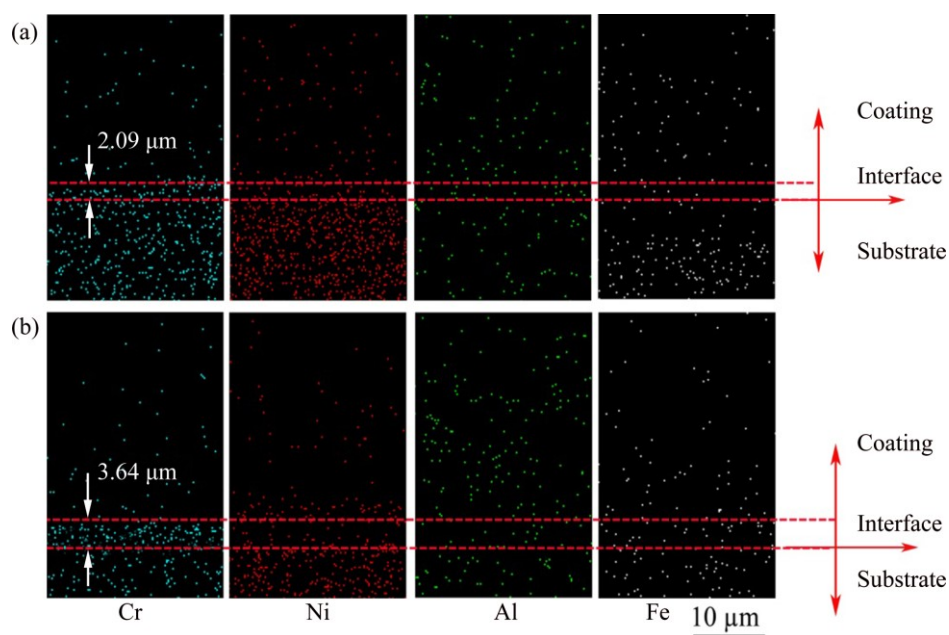


Fig. 6 Cross-sectional elemental distribution mapping of Cr, Ni, Al and Fe elements of non-BPs- (a) and BPs-coated (b) samples after isothermal oxidation in air at 1100 °C for 10 h

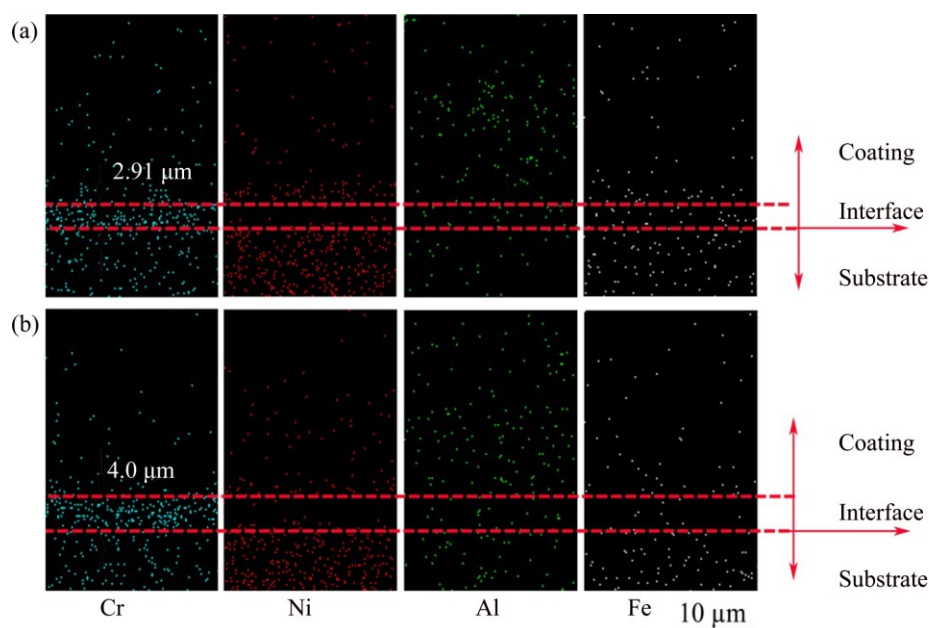


Fig. 7 Cross-sectional elemental distribution mapping of Cr, Ni, Al and Fe elements of non-BPs- (a) and BPs-coated (b) samples after isothermal oxidation in air at 1100 °C for 100 h

the Cr-rich transition-layer and composite coatings in oxidized coated samples, except in the narrow zone neighboring the coating–substrate interface which, visibly, is depleted of Ni (Figs. 6 and 7). As can be seen, the Cr-rich zone coincides with the zone depleted of nickel. These results indicate that chemical bonding might occur in the vicinity of the composite coatings–substrate interface.

To further identify the phase constitution of the interface region between YSZ/(Ni, Al) composite coatings and substrate, the cross-sectional micro-XRD

patterns of non-BPs- and BPs-coated samples after isothermal oxidation at 1100 °C in air for 10 h and 100 h, are illustrated in Figs. 8–10. In addition to the diffraction peaks of ZrO_2 , the peaks for CrO , Al_2O_3 and Cr–Ni phases are also revealed in both coated samples (Figs. 8 and 10). Due to the fact that the detection spot is situated near the coatings–substrate interface, it can be concluded that the XRD patterns of $Ni_{2.9}Cr_{0.7}Fe_{0.36}$ and $Ni_{0.1}Cr_{0.19}Fe_{0.7}$ phases originated from the substrate. Figures 9 and 10 indicate that the mixture phases of $Ni_{2.9}Cr_{0.7}Fe_{0.36}$ and $Ni_{0.1}Cr_{0.19}Fe_{0.7}$ occurred on the BPs-

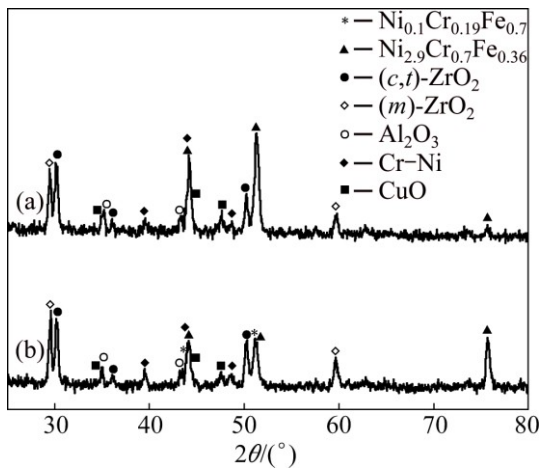


Fig. 8 Cross-sectional micro-XRD of non-BPs- (a) and BPs-coated (b) samples after isothermal oxidation in air at 1100 °C for 10 h

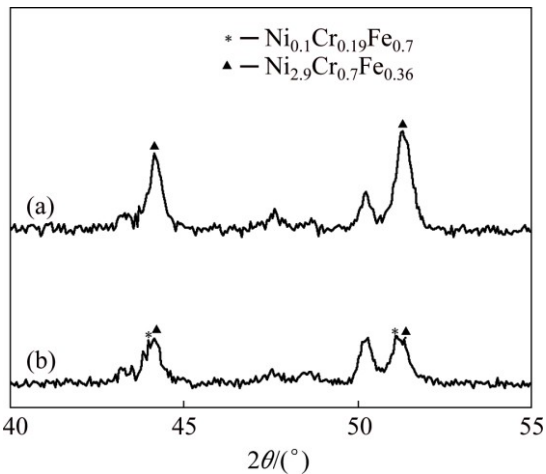


Fig. 9 Cross-sectional micro-XRD ($2\theta=40^{\circ}$ – 45°) of non-BPs- (a) and BPs-coated (b) samples after isothermal oxidation in air at 1100 °C for 10 h

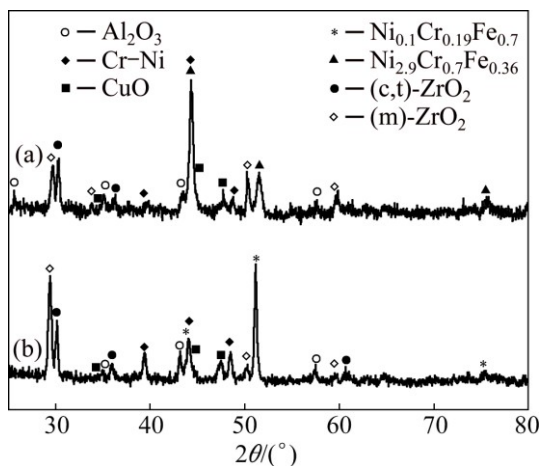


Fig. 10 Cross-sectional micro-XRD of non-BPs (a) and BPs-coated (b) samples after isothermal oxidation in air at 1100 °C for 100 h

coated samples after exposure in air. In contrast, only $\text{Ni}_{2.9}\text{Cr}_{0.7}\text{Fe}_{0.36}$ phase is detected on the non-BPs-coated samples after exposure in air. This suggests that Cr diffused out from the substrate to the coating resulted in phase transformation from $\text{Ni}_{2.9}\text{Cr}_{0.7}\text{Fe}_{0.36}$ to $\text{Ni}_{0.1}\text{Cr}_{0.19}\text{Fe}_{0.7}$ on the BPs substrate. These XRD results basically corroborate the SEM/EDS observations indicated in Figs. 6 and 7. Actually, the NiCrFe phase grains constitute an intermediate diffusion zone between the coating and the substrate. In addition, after isothermal oxidation in air at 1100 °C for 10 h, $(11\bar{1})_m$ monoclinic ZrO_2 diffraction peak began to appear, while the corresponding $(111)_{c,t}$ $(c,t)\text{-ZrO}_2$ diffraction intensity decreased (Fig. 8). When the oxidation time was increased to 100 h, $(11\bar{1})_m$ monoclinic ZrO_2 diffraction peak increased substantially, while the corresponding intensity for $(111)_{c,t}$ $(c,t)\text{-ZrO}_2$ diffraction peak was significantly decreased (Fig. 10), suggesting significant transformation of cubic/tetragonal to monoclinic during isothermal oxidation.

3.3 Adhesion strength of composite coatings

The adhesion strength curves of BPs- and non-BPs-coated samples as a function of the adhesion strength versus oxidation time at 1100 °C are depicted in Fig. 11. After vacuum sintering at 1100 °C for 2 h, the adhesion strengths of BPs- and non-BPs-coated samples are 4.5 N and 4.4 N, respectively. The adhesion strength increases in the initial oxidation for 10 h and reaches a maximum value to 4.8 N of BPs-coated samples and 4.6 N of non-BPs-coated samples. And then, the adhesion strength decreases with increasing oxidation time. With isothermal oxidation at 1100 °C for 100 h, the BPs-coated sample exhibits much higher adhesion strength about 3.3 N, which is about 26.9% that of the non-BPs-coated sample (2.6 N). This demonstrates that

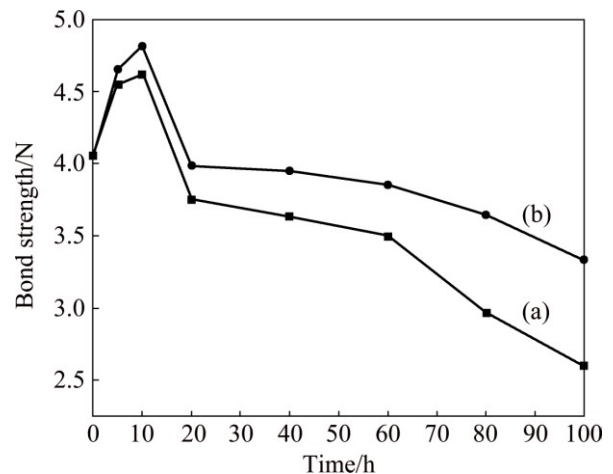


Fig. 11 Bond strength curves of BPs- (a) and non-BPs-coated (b) samples as function of bond strength versus oxidation time at 1100 °C

the BPs-coated samples have a better adhesion strength than non-BPs-coated samples after isothermal oxidation.

3.4 Oxidation resistance of composite coatings

Figure 12 shows the oxidation kinetic curves of non-BPs and BPs YSZ/(Ni, Al) composition coatings after isothermal oxidation at 1100 °C. The BPs-coated samples showed lower mass gain than that of the non-BPs-coated samples. For example, after 100 h exposure in air, the mass gain of the BPs-coated samples is 0.00559 mg/mm², which is lower than that of the non-BPs-coated samples (0.00817 mg/mm²). An identical increase trend of mass gain is observed for the both coated samples at the initial exposure period. However, the mass gain of the non-BPs-coated samples is much higher. These trends indicate that the BPs-coated samples have greater oxidation resistance as compared with the non-BPs-coated samples.

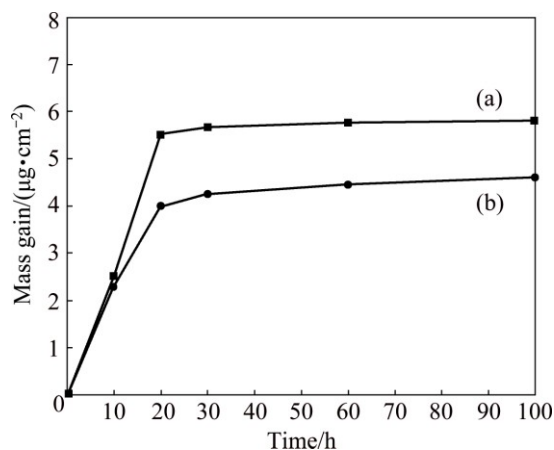


Fig. 12 Isothermal oxidation kinetics curves of non-BPs- (a) and BPs-coated (b) samples after isothermal oxidation at 1100 °C

4 Discussion

The analysis results listed above denote that ball peening of substrate not only results in the difference in microstructure of YSZ/(Ni, Al) composition coatings, but also leads to the variation of adhesion strength and high temperature oxidation resistance of the coatings through the surface modification of the substrate.

It has been proposed that steel surface condition can play a significant role in the number of supercritical nuclei formed [15]. Also, increasing substrate surface roughness tends to decrease the coating grain size and reduce the porosity of the coatings [16]. For YSZ/(Ni, Al) composition coatings deposited on the ball peened substrate, the ball peening treatment introduced a deformed layer with high density of crystalline defects on the surface of the substrate, which is beneficial to the crystallization and growth of YSZ coating according to

the crystallite theory. On the other hand, a larger surface roughness also promotes YSZ coatings to embed on the rough surface of substrate, which improved its adhesion strength.

Due to thermal expansion mismatch, residual thermal stresses develop during cooling of YSZ/(Ni, Al) composition coatings. Furthermore, the stress concentration factor at the sharp edges of the samples might contribute to minor cracking of the coating. It should be noted that, the ball peening treatment introduced high density of crystalline defects, which will absorb the residual thermal stress and lead to a markedly higher stress reduction on the BPs-coated samples. So, it is well understood that an undamaged coatings (no crack) occurred on the BPs-coated samples, whereas non-BPs-coated samples would be cracked, as shown in Fig. 2.

After vacuum sintering at 1100 °C for 2 h, more pores are homogeneously distributed on non-BPs-coated samples (Figs. 2(a) and (d)). As shown in Fig. 3, AlNi₃ phase formed on the both coated samples after vacuum sintering at 1100°C for 2 h. Accordingly, the local densification (volume shrinkage) due to the transformation of pure Al and pure Ni to AlNi₃ is the main reason of pore formation in the sintered composite coatings [17]. Furthermore, under current vacuum sintering condition (1100 °C in vacuum), the evaporation of melted Al particles and the bigger diffusion coefficient of Ni than that of Al, which will contribute to the Kirkendall pore formation. It can also be seen that the mass fraction of AlNi₃ phase for the non-BPs-coated samples is higher than that of the BPs-coated samples (Fig. 3). The generation of AlNi₃ phase releases a lot of heat and melting of inter-metallic. While cooling the coated samples, there is inter-metallic liquid–solid contraction, so the pore is formed.

Plastic deformation may influence diffusivities in a material by increasing dislocation [11–13]. It is believed that the ball peening treatment caused more defects to form at the grain boundaries of the substrate. These grain and grain boundary defects acted as fast diffusion paths for Cr atoms in the substrate. The selective long-range migration of Cr (Figs. 6 and 7), in spite of its low diffusion coefficients (compared with Fe and Ni), suggests the existence of a stronger chemical driving force in the system. Under finite partial pressure of oxygen, it may be assumed that CrO clusters are formed in the composite coatings due to dissolution of the substrate, as revealed by XRD analysis indicated in Figs. 8 and 10. According to NAIDICH [18], metal–oxygen clusters such as CrO acquire an ionic-covalent character due to charge transferring from metal to oxygen. These clusters can adsorb strongly on the surface of an ionic-covalent ceramic (e.g., ZrO₂) due to Coulombic interaction. The interaction of CrO clusters is expected to

be stronger than that of NiO or FeO owing to the higher degree of ionicity. Therefore, Cr enrichment at the ZrO₂–substrate interface may be the adsorption of CrO cluster in the composite coating during isothermal oxidation at 1100 °C. During subsequent oxidation, the presence of the diffusion flux of Cr through the substrate and oxygen from the atmosphere drives the following equation in the forward direction:



The Cr-rich zones formed at the interface act for this reaction.

McCARRON et al [19] have reported AlNi₃ to be NiO former. According to NATESAN [20], the oxidation of AlNi₃ at 900 °C and above produces scales containing an outer layer of NiO, an inner layer of Al₂O₃ and an intermediate layer of the Ni–Al spinel NiAl₂O₄. Their oxidation mechanism can be as follows. At the very earlier stage of oxidation, oxides of all elements will be formed. Assuming an oxidation mode of grain-to-grain, a mixture layer of Al₂O₃, Cr₂O₃ and NiO will form. As the mixture layer becomes thicker, the outward diffusion of Al may gradually become sufficient to sustain the growth of alumina, while the oxygen partial pressure at the oxide–coating interface can be decreased down to low enough that Cr₂O₃ and NiO become unstable. Then a continuous alumina layer will be established, according to the selective oxidation mechanism. The outermost mixture layer of oxides can be very thin, and it contains alumina too, so they cannot be distinguishable from the alumina scale in the analysis of XRD.

XRD analysis (Fig. 4 and Ref. [10]) indicates that the scale formed on the non-BPs-coated samples consists of Al₂O₃, whereas NiO is observed on BPs-coated samples after 10 h isothermal oxidation at 1100 °C. This means that the diffusion coefficient of Al on the BPs-coated samples is lower than that on the non-BPs-coated samples. The oxidation activation energies are known to remain constant [21] and the diffusion coefficient of Al for a similar composition shows that the activation energy actually remains constant at the temperature of 900–1200 °C [22]. Accordingly, the effect on microstructure of coating is considered to be an effect of diffusion activation energy [23].

The current non-BPs-coated samples contain large volume fractions of pores of micron level diameter, as shown in Fig. 2. The pores in the coatings not only increase the exposed surface area but also enhance stress in the presence of stress. Residual stresses are commonly generated in the coatings due to the growth of oxide scale and the thermal cycling. It has been suggested that stress could modify transient oxidation rates, and promote the faster formation of Al₂O₃ in contrast to mixed oxide spinels [24]. Since the stress generally

causes the scales to be thinner, faster diffusion of Al to the coating surface to form a more protective layer is implied. More surface area is covered with Al₂O₃ layer which suppresses nucleation of NiO. Thus, only Al₂O₃ can be identified by XRD analysis on the surface of the non-BPs-coated samples in the early of oxidation. In further oxidation, for the coating adjacent to the scale, the depletion of Al due to the formation of Al₂O₃ caused the inward diffusion of Ni to form NiAl₂O₃ phase. Thus, the formation of non-protective scale mainly induces the poor oxidation resistance of the non-BPs-coated samples. Furthermore, due to high pore density on the non-BPs-coated samples, active path of diffusion is readily formed between the oxidized and non-oxidized pores, allowing inward of oxygen. This is evidenced in Figs. 2(b) and (c), where the oxide layer appears defective, probably as a result of cracking of oxide scale and/or oxidized channels between pores by high residual stresses. The cracks will increase the direct exposure of the coating to oxygen, which will result in fairly higher mass change of the coating, as observed in Fig. 12(a).

In contrast, the BPs coatings contain few smaller irregular pores (Figs. 2(d)–(f)), the reduction of pores in BPs-coated samples greatly decreases the stress concentration on the coatings. Therefore, an improvement in oxidation resistance of the coatings can be expected. It is believed that the oxidation kinetics of the coatings at an initial period is controlled by the NiO growth due to fast diffusion of Ni. Thus, NiO can be identified by XRD analysis on the surface of the BPs-coated samples in the early of oxidation. With thickening of the oxide scale, the inward flux of oxygen is reduced further, which is beneficial to the preferential oxidation of Al, leading to an innermost layer of Al₂O₃ next to the surface of the coatings. The formation of a thin and dense Al₂O₃ layer resulted in an improvement of oxidation resistance of the BPs-coated samples (Fig. 12(b)).

When the Al concentration reaches a critical minimum value, NiO, Cr₂O₃ will be formed. The spinel of NiCr₂O₄ is produced by the reaction of NiO with Cr₂O₃. In addition, as shown in Figs. 6 and 7, the substrate and the coating are separated by a Cr layer, which may enhance the spallation resistance [25]. Combining chemical composition analysis (Figs. 6 and 7) and XRD (Figs. 8–10) results, it can be concluded that an active of NiCrO layer is applied to the Inconel 600 superalloy/YSZ/(Ni, Al) composite coating system. NiCr is more ductile than Cr, so it may be more beneficial to the adhesion strength and spallation resistance of the coating system.

The *m*-ZrO₂ phase is detected on both coated samples during isothermal oxidation (Figs. 8–10). The phase transformation of *t*-phase to *m*-phase will bring

about a significant volume expansion, which is accompanied by the formation of small cracks and consequently reduces the mechanical properties of TBCs, and caused the adhesion strength to decrease with increasing oxidation time. However, it seems that the amount of formed $m\text{-ZrO}_2$ is not sufficient to accelerate degradation.

5 Conclusions

1) After vacuum sintering at 1100 °C for 2 h, a number of micron and submicron pores are homogeneously distributed on non-BPs-coated samples. Subsequently, after isothermal oxidation at 1100 °C for 10 h and 100 h in air, some big cracks can be seen in the non-BPs-coated samples. In contrast, the BPs coatings contain smaller irregular pores and show an excellent adherence to the substrate without cracks or spallation.

2) After isothermal oxidation at 1100 °C, an obvious outward diffusion of Cr from the substrate into the coatings takes place due to the chemical reaction of O and Cr. An active of NiCrO layer is applied to the Inconel 600 superalloy/ YSZ/(Ni, Al) composite coating system.

3) The BPs-coated samples have superior adhesion strength and high temperature oxidation resistance compared with the non BPs-coated samples.

References

- [1] SMITH P J R, TAYLOR M P, EVANS H E, MURRAY N E, McMILLAN C, CHERRINGTON J. The oxidation and interdiffusion of a chromia forming multilayered TBC system [J]. *Oxidation of Metals*, 2014, 81: 47–55.
- [2] MUNAWAR A U, SCHULZ U, CERRI G, LAU H. Microstructure and cyclic lifetime of Gd and Dy-containing EB-PVD TBCs deposited as single and double-layer on various bond coats [J]. *Surface and Coatings Technology*, 2014, 245: 92–101.
- [3] CHIRIVI L, NICHOLLS J R. Influence of surface finish on the cyclic oxidation lifetime of an EB-PVD TBC, deposited on PtAl and Pt-diffused bond coats [J]. *Oxidation of Metals*, 2014, 81: 17–31.
- [4] LU Z, KIM M S, MYOUNG S W, LEE J H, JUNG Y G, KIM I S, JO C Y. Thermal stability and mechanical properties of thick thermal barrier coatings with vertical type cracks [J]. *Transactions of Nonferrous Metals Society of China*, 2014, 24: 29–35.
- [5] JIA Sheng-kai, ZOU Yong, XU Ji-yuan, WANG Jing, YU Lei. Effect of TiO_2 content on properties of Al_2O_3 thermal barrier coatings by plasma spraying [J]. *Transactions of Nonferrous Metals Society of China*, 2015, 25: 175–183.
- [6] BAI Ming-wen, GUO Fang-wei, XIAO Ping. Fabrication of thick YSZ thermal barrier coatings using electrophoretic deposition [J]. *Ceramics International*, 2014, 40: 16611–16616.
- [7] MOHAN P, YAO B, PATTERSON T, SOHN Y H. Electrophoretically deposited alumina as protective overlay for thermal barrier coatings against CMAS degradation [J]. *Surface and Coatings Technology*, 2009, 204: 797–801.
- [8] MALEKI-GHALEH H, REKABESLAMI M, SHAKERI M S, SIADATI M H, TALEBIAN S H, AGHAJANI H. Nano-structured yttria-stabilized zirconia coating by electrophoretic deposition [J]. *Applied Surface Science*, 2013, 280: 666–672.
- [9] WANG Z, XIAO P, SHEMIT J. Fabrication of composite coatings using a combination of electrochemical methods and reaction bonding process [J]. *Journal of the European Ceramic Society*, 2000, 20: 1469–1473.
- [10] LI Chun-ling, WANG Wei, TAN Shi-lei, SONG Shan-guang. Bond strength and oxidation resistance of YSZ/(Ni, Al) composite coatings [J]. *Surface Engineering*, 2014, 30: 619–623.
- [11] AHMED A A, MHAEDE M, WOLLMANN M, WAGNER L. Effect of surface and bulk plastic deformation on the corrosion resistance and corrosion fatigue performance of AISI 316L [J]. *Surface and Coatings Technology*, 2014, 259: 448–455.
- [12] MARK H, BENJAMIN J L, ORGUN A G, PAUL M N, ZORAN S F. The impact of a magnesium zirconate thermal barrier coating on homogeneous charge compression ignition operational variability and the formation of combustion chamber deposits [J]. *International Journal of Engine Research*, 2015, 16: 968–981.
- [13] ARIFVIANTOR B, SUYITNO. Surface roughness and wettability of AISI 316L induced by surface mechanical attrition treatment with different milling ball diameter [C]//International Conference on Instrumentation, Communication, Information Technology, and Biomedical Engineering. Piscataway: Institute of Electrical and Electronics Engineers, 2009.
- [14] CHUNG F H. Quantitative interpretation of X-ray diffraction patterns of mixtures. II. Adiabatic principle of X-ray diffraction analysis of mixtures [J]. *Journal of Applied Crystallography*, 1974, 7: 526–531.
- [15] STRUTZENBERGER J, FADERL J. Solidification and spangle formation of hot-dip-galvanized zinc coatings [J]. *Metallurgical and Materials Transactions A*, 1988, 29: 631–646.
- [16] KABOLIC S, MCDERMID J R. Effect of process variables on the grain size and crystallographic texture of hot-dip galvanized coatings [J]. *Metallurgical and Materials Transactions A*, 2014, 45: 3938–3953.
- [17] SUSAN D F, MISIOLEK W Z, MARDER A R. Reaction synthesis of Ni–Al-based particle composite coatings, metall [J]. *Metallurgical and Materials Transactions A*, 2001, 32: 379–390.
- [18] NAIDICH J V. Progress in surface and membrane science [M]. 2nd ed. New York: Academic Press, 1981: 353–484.
- [19] McCARRON R L, LINDBLAD N R, CHATTERJI D. Environmental resistance of pure and alloyed $\gamma\text{-Ni}_3\text{Al}$ and $\beta\text{-NiAl}$ [J]. *Corrosion*, 1976, 32: 476–481.
- [20] NATESAN K. Oxidation-sulfidation behavior of Ni aluminide in oxygen-sulfur mixed-gas atmospheres [J]. *Oxidation of Metals*, 1988, 30: 53–83.
- [21] ENGSTROM A, MORRAL J E, AGREN J. Computer simulations of Ni–Cr–Al multiphase diffusion couples [J]. *Acta Materialia*, 1997, 45: 1189–1199.
- [22] RENUSCH D, SCHORR M, SCHUTZE M. The role that bond coat depletion of aluminum has on the lifetime of APS-TBC under oxidizing conditions [J]. *Materials and Corrosion*, 2008, 59: 547–555.
- [23] SALAM S, HOU P Y, ZHANG Y D, WANG H F, ZHANG C, YANG Z G. Compositional effects on the high-temperature oxidation lifetime of MCrAlY type coating alloys [J]. *Corrosion Science*, 2015, 95: 143–151.
- [24] BARNARD B R, LIAW P K, BUCHANAN R A, KLARSTROM D L. Affects of applied stresses on the isothermal and cyclic high-temperature oxidation behavior of superalloys [J]. *Materials Science and Engineering A*, 2010, 527: 3813–3821.
- [25] HOU S J, ZHU S L, ZHANG T, WANG F H. A magnetron sputtered microcrystalline $\beta\text{-NiAl}$ coating for SC superalloys. Part I. Characterization and comparison of isothermal oxidation behavior of at 1100 °C with a NiCrAlY [J]. *Applied Surface Science*, 2015, 324: 1–12.

基体喷丸处理对电泳沉积 YSZ/(Ni, Al)热障复合涂层 显微组织、相变和性能的影响

宋闪光, 谭世磊, 戚哮啸, 王伟, 王莉莉

上海工程技术大学 材料工程学院, 上海 201620

摘要: 采用电泳沉积技术在喷丸处理和未处理的 Inconel600 高温合金基体表面制备 YSZ/(Ni,Al)热障复合涂层, 然后进行真空烧结。使用 X 射线衍射、扫描电子显微镜和电子探针能谱仪分析复合涂层的组成和相变, 分析和讨论基体喷丸处理后的 YSZ/(Ni,Al)热障复合涂层的显微组织结构和性能之间的关系。结果显示, 基体喷丸处理后的 YSZ/(Ni,Al)热障复合涂层在 1100 °C 等温氧化 100 h 后的结合强度和抗氧化增重分别是 3.3 N 和 0.00817 mg/cm², 而基体未处理的 YSZ/(Ni,Al)热障复合涂层的结合强度和抗氧化增重分别为 2.6 N 和 0.00559 mg/cm²。在能谱分析得出喷丸处理的涂层在等温氧化后出现明显的铬元素从基体向涂层扩散。基体喷丸处理后的 YSZ/(Ni,Al)热障复合涂层具有更优异的结合性能和抗高温氧化性能。

关键词: 复合涂层; 电泳沉积; 喷丸处理; 结合力; 抗高温氧化

(Edited by Xiang-qun LI)